Systematic variation of spin-orbit coupling with d-orbital filling: Large inverse spin Hall effect in 3d transition metals

Chunhui Du, Hailong Wang, Fengyuan Yang, and P. Chris Hammel

Phys. Rev. B **90**, 140407 — Published 31 October 2014

DOI: 10.1103/PhysRevB.90.140407

Surprisingly large inverse spin Hall effect and systematic variation of spin-orbit coupling with *d*-orbital filling in 3*d* transition metals

Chunhui Du[†], Hailong Wang[†], Fengyuan Yang[*], and P. Chris Hammel[*]

Department of Physics, The Ohio State University, Columbus, OH, 43210, USA

[†]These authors made equal contributions to this work

[*]Emails: fyyang@physics.osu.edu; hammel@physics.osu.edu

Abstract

It is generally believed that spin-orbit coupling (SOC) follows Z^4 (atomic number) dependence and becomes significant only in heavy elements. Consequently, SOC in 3*d* transition metals should be negligible given their small *Z*. Using dynamic spin pumping of $Y_3Fe_5O_{12}$-based structures, we uncover a systematic evolution of spin Hall angle (θ_{SH}) with *d*-orbital filling in a series of 3*d* metals, reminiscent of behavior observed in 5*d* metals. In particular, Cr and Ni show very large θ_{SH} (half of that for Pt), indicating that *d*-orbital filling rather than *Z* plays a dominant role in spin Hall effect (SHE) in 3*d* metals. This result enriches our understanding of SHE and broadens the scope of materials available for exploring the rich phenomena enabled by SOC as well as presenting a guidepost for testing theoretical models of spin-orbit coupling in transition metals.

PACS: 75.47.Lx, 76.50.+g, 75.70.Ak, 61.05.cp

Spin-orbit coupling is the underlying mechanism for magnetocrystalline anisotropy [1], anomalous Hall effect [2], and more recently, spin Hall effect [3] and topological insulators [4]. It is generally believed that SOC varies as Z^4 [5-7], implying that SOC is important only in heavy elements, while in lighter elements such as 3*d* transition metals, SOC should be negligibly small. SHE depends on the SOC and θ_{SH} is a measure of the strength of SOC. Because of the generally accepted Z^4 dependence of SOC, measurement of θ_{SH} has been focused on heavy elements by SHE [8] or inverse spin Hall effect (ISHE) [9-15], while 3*d* metals have rarely been studied [16, 17].

Ferromagnetic resonance (FMR) spin pumping of pure spin currents from a ferromagnet (FM) into a nonmagnetic (NM) material provides a powerful technique for measurement of θ_{SH} in a broad range of materials [7, 9]. We report a systematic study of the ISHE in a series of 3*d* transition metals using FMR spin pumping from $Y_3Fe_5O_{12}$ (YIG) epitaxial films into Ti, V, Cr, Mn, $Fe_{50}Mn_{50}$ (FeMn), $Fe_{20}Ni_{80}$ (Py), Ni, and Cu. The large ISHE signals in our YIG-based structures [7, 15, 18-21] provides unprecedented sensitivity for characterizing the ISHE in 3*d* metals which are expected to have weak SOC. Surprisingly, we detect an ISHE voltage (V_{ISHE}) exceeding 5 mV in a YIG/Cr(5 nm) bilayer, which is among the highest V_{ISHE} we observed in any materials [7, 15].

We deposit epitaxial YIG films on (111)-oriented $Gd_3Ga_5O_{12}$ (GGG) substrates [7, 15, 22]. A 2θ-ω x-ray diffraction (XRD) scan of a 25-nm YIG film shown in Fig. 1(a) shows clear Laue oscillations. The x-ray reflectometry (XRR) spectrum of a 40-nm YIG film in Fig. 1(b) reflects the smooth YIG surface. The atomic force microscopy (AFM) image in the inset to Fig. 1(b) exhibits a roughness of only 0.106 nm. Figure 1(c) shows the derivative of a FMR absorption spectrum for a 20-nm YIG film taken in a FMR cavity at a radio-frequency (rf) f =

9.65 GHz and a microwave power P_{rf} = 0.2 mW, which gives a peak-to-peak linewidth (ΔH) of 9.5 Oe. Spin pumping measurements are carried out at room temperature on YIG/metal bilayers (approximate dimensions of 1 mm × 5 mm). A DC magnetic field ***H*** is applied in the *xz*-plane and the ISHE voltage is measured across the ~5-mm long metal layer along the *y*-axis, as illustrated in Fig. 1(d).

Figures 2(a) to 2(f) show V_{ISHE} vs. H - H_{res} spectra (H_{res} is the resonance field of the YIG) of YIG/metal(10 nm) bilayers for Ti, V, Cr, Mn, FeMn, and YIG/Cu(10 nm)/Ni(10 nm) trilayer at two opposite in-plane field orientations θ_H = 90° and 270° using P_{rf} = 200 mW, which exhibit V_{ISHE} = -24.6 μV, -594 μV, -2.55 mV, -549 μV, -4.65 μV, and 39.4 μV, respectively, at θ_H = 90°. The negative sign in V_{ISHE} arises from the convention of positive V_{ISHE} for YIG/Pt at θ_H = 90°. The strong exchange coupling between YIG and Ni induces such substantial additional damping of the YIG that we use YIG/Cu/Ni trilayers to determine θ_{SH} as reported previously [21]. The 2.5-mV ISHE signal measured in YIG/Cr(10 nm) is exceptionally large and comparable to the values detected in 5*d* metals Ta, W, and Pt on our YIG films [7, 15]. This suggests unexpectedly large θ_{SH} and surprisingly strong SOC in Cr. Given the relatively small Z of 3*d* elements, we explore the potential role of *d*-orbital configuration and antiferromagnetism (AF), e.g., in Cr and FeMn, [23] in this surprising result. The detailed study of eight 3*d* transition metals [7, 21] presented here uncovers unexpected role of *d*-orbital filling in spin Hall physics in this group of light materials.

The mV-level V_{ISHE} observed in YIG/Cr is surprising since the SOC in Cr (Z = 24) has been considered negligible. θ_{SH} is a measure of SOC and can be calculated from [9, 10, 12, 14],

$$V_{ISHE} = -e\theta_{SH} w R \lambda_{SD} \tanh\left(\frac{t_{NM}}{2\lambda_{SD}}\right) g^{\uparrow\downarrow} f P \left(\frac{\gamma h_{rf}}{4\pi\alpha f}\right)^2, \quad (1)$$

where e is the electron charge, w, R and t_{NM} are the sample width, resistance and thickness,

respectively, of the Cr layer, λ_{SD} is the spin diffusion length of Cr, $g^{\uparrow\downarrow}$ is the interfacial spin mixing conductance, P = 1.21 is a factor arising from the ellipticity of the magnetization precession [7], $\gamma$is the gyromagnetic ratio, h_{rf} = 0.25 Oe is the rf field at P_{rf} = 200 mW [7], and α is the Gilbert damping constant of YIG. To calculate θ_{SH}, we first determine λ_{SD} from the Cr thickness (t_{Cr}) dependence of V_{ISHE} [Fig. 2(g)], which is partially due to the variation in resistivity (ρ) of the Cr films [Fig. 2(h)] similar to the behavior reported previously [24]. The ISHE-induced charge current $I_c = V_{ISHE}/R$ is proportional to the spin current pumped into Cr [7, 15]. Figure 2(i) plots the t_{Cr} dependence of V_{ISHE}/Rw, from which we obtain λ_{SD} = 13.3 ± 2.1 nm by fitting to $\frac{V_{ISHE}}{Rw} \propto \lambda_{SD}\tanh\left(\frac{t_{Cr}}{2\lambda_{SD}}\right)$ [25]. $g^{\uparrow\downarrow}$ can be obtained from the spin-pumping enhancement of damping [9-12],

$$g^{\uparrow\downarrow} = \frac{4\pi M_s t_{YIG}}{g\mu_B}(\alpha_{YIG/NM} - \alpha_{YIG}), \quad (2)$$

where g, μ_B, and t_{YIG} are the Landé factor, Bohr magneton, and YIG thickness, respectively. We determine the damping constants of a bare YIG film (α_{YIG}) and a YIG/Cr bilayer ($\alpha_{YIG/NM}$) from the frequency dependencies of the FMR linewidth measured using a microstrip transmission line [Fig. 3(a)]. The linewidth increases linearly with frequency: $\Delta H = \Delta H_{inh} + \frac{4\pi\alpha f}{\sqrt{3}\gamma}$ [26], where ΔH_{inh} is the inhomogeneous broadening. Table I shows the damping enhancement due to spin pumping: $\alpha_{sp} = \alpha_{YIG/NM} - \alpha_{YIG}$, where $\alpha_{YIG/NM}$ and α_{YIG} = (8.7 ± 0.6) × 10^{-4} are obtained from the least-squares fits in Fig. 3(a). Thus, we calculate $g^{\uparrow\downarrow}$ = (8.3 ± 0.7) × 10^{17} m^{-2} for the YIG/Cr interface and θ_{SH} = -0.051 ± 0.005 for Cr. This surprisingly large θ_{SH} is half the value of Pt [7].

Using the same approach, we obtain θ_{SH} for other 3*d* metals. The spin diffusion lengths of V, Mn, and Ni are determined to be 14.9 ± 2.4, 10.7 ± 1.1, and 3.2 ± 0.1 nm as shown in Figs.

2(j), 2(k), and 2(l), respectively. Considering that V, Cr, and Mn all have similar spin diffusion lengths, and since θ_{SH} is virtually insensitive to λ_{SD} when $\lambda_{SD} \geq t_{NM}$ [due to the term $\lambda_{SD}\tanh\left(\frac{t_{NM}}{2\lambda_{SD}}\right)$ in Eq. (2)], it is safe to assume λ_{SD} of Ti is similar to Cr. The calculated values of θ_{SH} for Ti and Mn are very small (Table I) while the spin Hall angles for V and Ni are quite large for 3*d* metals.

To highlight the systematic behavior of θ_{SH}, we plot θ_{SH} vs. *Z* in Fig. 3(b) for the eight 3*d* metals. We note that V, Cr, and Ni with large θ_{SH} sit directly above Ta, W, and Pt in the periodic table, respectively, which exhibit some of the largest θ_{SH}. This suggests that the *d*-electron configuration of the transition metals plays a very important role in SHE, consistent with the prediction of Tanaka *et al*. [27] who illuminated the role of the total number of 4*d* (5*d*) and 5*s* (6*s*) electrons in the SHE in the 4*d* (5*d*) metals. To understand the role of *d*-electrons, we list in Table I the total number of 3*d* and 4*s* electrons, n_{3d+4s}. We note that θ_{SH} varies significantly both in sign and magnitude: θ_{SH} is negative from Ti (n_{3d+4s} = 4) to FeMn (n_{3d+4s} = 7.5) and changes to positive for Py (n_{3d+4s} = 9.6), Ni (n_{3d+4s} = 10) and Cu (n_{3d+4s} = 11) while its magnitude reaches maximum at Cr (n_{3d+4s} = 6) and Ni (n_{3d+4s} = 10). The sign change in θ_{SH} mimics the trend observed in 5*d* metals [7, 13, 27, 28], while the magnitude of θ_{SH} spans a range of almost three orders of magnitude. From Fig. 3(b) and our previous result on 5*d* metals [7], we can gain insights into the underlying mechanisms responsible for the SHE and SOC in transition metals.

There are three mechanisms that could be responsible for SHE in transition metals: 1) atomic number, 2) *d*-electron count, and 3) magnetic ordering; we address these separately below. First, while the atomic number may play a role in SHE in 3*d* metals, it is not a dominant factor: for example, between Cr and W which belong to the same VIB transition metal group, the

Z^4 dependence predicts a difference of 90 times in their SOC strengths and θ_{SH}, while our experimental values show a factor of 2.7 in θ_{SH} between the two elements.

Secondly, we can also rule out magnetic ordering in the 3*d* metals as the dominant factor. While Cr and Ni exhibit large θ_{SH}, they also possess magnetic ordering: Cr is an AF [23] and Ni is a FM. To probe the role of AF ordering in ISHE in 3*d* metals, we compare the spin Hall angles of Cr and FeMn, a robust AF. The θ_{SH} of Cr is 689 times larger than that of FeMn (Table I). The dramatic difference in the two 3*d* AF metals suggests that the surprisingly large θ_{SH} in Cr does not arise from its AF order [29]. The very small θ_{SH} of FeMn also agrees with the theoretical prediction for 4*d* and 5*d* metals [27] in that at $n_{3d+4s} \approx 7.5$, the spin Hall conductivity (SHC) crosses zero.

For FM metal Ni, we consider the two elements directly below Ni in the periodic table, Pd and Pt. Tanaka *et al*. [27] calculate that the SHC of Pd is ~70% of that for Pt, much larger than the 11% predicted from the Z^4 dependence. If we similarly assume a 70% ratio in SHC for Ni relative to Pd, we would conclude that the SHC for Ni is 49% that of Pt: very close to our experimentally measured ratio. This is without considering the FM ordering in Ni. Thus, the surprisingly large values and significant variation in θ_{SH} of 3*d* metals arise mainly from the *d*-electron configuration, indicating its dominant role in spin Hall physics [7, 13, 27, 28].

Taken together, our results in 3*d* and 5*d* [7] metals reveal a surprising feature of ISHE: the effects of atomic number and *d*-orbital filling are additive—not multiplicative—indicating they operate independently, and each of these mechanisms can be of comparable importance. This means that if either contribution (*Z* or *d*) is large, the SHE is large, not that if either one is small, the SHE is small. For example, the Z^4 dependence is clearly dominant in the Cu, Ag, and Au series [7] whose filled *d*-shells have zero orbital moment and do not contribute to the ISHE;

while for transition metals with partially filled *d*-orbitals, the *d*-orbital contribution to the ISHE is dominant, as demonstrated by the variation of sign and magnitude of θ_{SH} in both 3*d* and 5*d* transition metals.

Furthermore, we confirm the influence of Cr antiferromagnetism on the static and dynamic magnetization of YIG. Cr is an incommensurate AF with a Néel temperature of 311 K in the bulk [23]. In Cr thin films, the AF ordering temperature is reduced. The static or dynamic AF ordered spins in Cr are expected to couple to the YIG magnetization via interfacial exchange interaction [30], resulting in possible exchange bias and enhanced coercivity (H_c) [31]. The room temperature, in-plane magnetic hysteresis loops for a 20-nm YIG film and YIG/Cr(t_{Cr}) bilayers with t_{Cr} = 10, 35, 50, and 100 nm shown in Fig. 4 demonstrate that this is in fact the case. The bare YIG film exhibits a square hysteresis loop with a very small H_c = 0.35 Oe and a very sharp magnetic switching. At t_{Cr} = 10 nm, H_c only increases slightly to 0.52 Oe, suggesting that at 10 nm, the correlation of Cr spins is fairly weak. As t_{Cr} increases, H_c continuously rises and reaches 1.73 Oe, indicating strengthening AF correlation with increasing t_{Cr}. This observation is further verified by the magnetic damping enhancement shown in the inset to Fig. 4, where the YIG/Cr(100 nm) exhibits a much larger damping constant than the YIG/Cr(10 nm). As a comparison, both the 10-nm and 100-nm vanadium films induce similar damping in YIG due to its nonmagnetic nature.

In conclusion, we observe surprisingly large, mV-level ISHE voltages in YIG/Cr bilayers and robust spin pumping signals in other 3*d* metals. By measuring ISHE voltages and damping enhancement, we determine the spin Hall angles of eight 3*d* metals, which reveal unexpected systematic behavior involving both sign change and dramatic variation in magnitude, implying the dominant role of *d*-electron configuration in SHE of 3*d* metals. Theoretical calculations

similar to those performed for 4*d* and 5*d* transition metals [27] are needed for thorough understanding of the underlying mechanisms responsible for the observed large SHE in 3*d* transition metals.

This work was primarily supported by the U.S. Department of Energy (DOE), Office of Science, Basic Energy Sciences, under Award# DE-FG02-03ER46054 (FMR and spin pumping characterization) and Award# DE-SC0001304 (sample synthesis and magnetic characterization). This work was supported in part by the Center for Emergent Materials, an NSF-funded MRSEC under award # DMR- 1420451 (structural characterization). Partial support was provided by Lake Shore Cryogenics Inc. and the NanoSystems Laboratory at the Ohio State University.

Reference:

1. P. Bruno, *Phys. Rev. B* **39**, 865(R) (1989).
2. N. Nagaosa, J. Sinova, S. Onoda, A. H. MacDonald, and N. P. Ong, *Rev. Mod. Phys.* **82**, 1539 (2010).
3. J. E. Hirsch, *Phys. Rev. Lett*. **83**, 1834 (1999).
4. X.-L. Qi and S.-C. Zhang, *Rev. Mod. Phys*. **83**, 1057 (2011).
5. Y. Tserkovnyak, A. Brataas, G. E. W. Bauer, and B. I. Halperin, *Rev. Mod. Phys.* **77**, 1375 (2005).
6. D. D. Sarma, *Proc. Indian Acad. Sci (Chem. Sci.)* **90**, 19 (1981).
7. H. L. Wang, C. H. Du, Y. Pu, R. Adur, P. C. Hammel, and F. Y. Yang, *Phys. Rev. Lett*. **112**, 197201 (2014).
8. L. Liu, C. F. Pai, Y. Li, H. W. Tseng, D. C. Ralph, R. A. Buhrman, *Science* **336**, 555 (2012).
9. O. Mosendz, V. Vlaminck, J. E. Pearson, F. Y. Fradin, G. E. W. Bauer, S. D. Bader, and A. Hoffmann, *Phys. Rev. B* **82**, 214403 (2010).
10. F. D. Czeschka, L. Dreher, M. S. Brandt, M. Weiler, M. Althammer, I.-M. Imort, G. Reiss, A. Thomas, W. Schoch, W. Limmer, H. Huebl, R. Gross, and S. T. B. Goennenwein, *Phys. Rev. Lett*. **107**, 046601 (2011).
11. B. Heinrich, C. Burrowes, E. Montoya, B. Kardasz, E. Girt, Y.-Y. Song, Y. Y. Sun, and M. Z. Wu, *Phys. Rev. Lett*. **107**, 066604 (2011).
12. E. Shikoh, K. Ando, K. Kubo, E. Saitoh, T. Shinjo, and M. Shiraishi, *Phys. Rev. Lett.* **110**, 127201 (2013).
13. D. Qu, S. Y. Huang, B. F. Miao, S. X. Huang, and C. L. Chien, *Phys. Rev. B* **89**, 140407(R) (2014).

14. C. Hahn, G. de Loubens, O. Klein, M. Viret, V. V. Naletov, and J. Ben Youssef, *Phys. Rev. B* **87**, 174417 (2013).

15. H. L. Wang, C. H. Du, Y. Pu, R. Adur, P. C. Hammel, and F. Y. Yang, *Phys. Rev. B* **88**, 100406(R) (2013).

16. B. F. Miao, S. Y. Huang, D. Qu, and C. L. Chien, *Phys. Rev. Lett.* **111**, 066602 (2013).

17. A. Tsukahara, Y. Ando, Y. Kitamura, H. Emoto, E. Shikoh, M. P. Delmo, T. Shinjo, and M. Shiraishi, *Phys. Rev. B* **89**, 235317 (2014).

18. C. H. Du, H. L. Wang, Y. Pu, T. L. Meyer, P. M. Woodward, F. Y. Yang, and P. C. Hammel, *Phys. Rev. Lett.* **111**, 247202 (2013).

19. C. H. Du, H. L. Wang, F. Y. Yang, and P. C. Hammel, *Phys. Rev. Applied* **1**, 044004 (2014).

20. H. L. Wang, C. H. Du, P. C. Hammel, and F. Y. Yang, *Phys. Rev. B* **89**, 134404 (2014).

21. H. L. Wang, C. H. Du, P. C. Hammel, and F. Y. Yang, *Appl. Phys. Lett.* **104**, 202405 (2014).

22. C. H. Du, R. Adur, H. L. Wang, A. J. Hauser, F. Y. Yang, and P. C. Hammel, *Phys. Rev. Lett.* **110**, 147204 (2013).

23. F. Y. Yang and C. L. Chien, *Phys. Rev. Lett*. **90**, 147201 (2003).

24. A. K. Kulkarni and L. C. Chang, *Thin Solid Films* **301**, 17 (1997).

25. H. Nakayama, K. Ando, K. Harii, T. Yoshino, R. Takahashi, Y. Kajiwara, K. Uchida, Y. Fujikawa, and E. Saitoh, *Phys. Rev. B* **85**, 144408 (2012).

26. S. S. Kalarickal, P. Krivosik, M. Z. Wu, C. E. Patton, M. L. Schneider, P. Kabos, T. J. Silva, and J. P. Nibarger, *J. Appl. Phys.* **99**, 093909 (2006).

27. T. Tanaka, H. Kontani, M. Naito, T. Naito, D. S. Hirashima, K. Yamada, and J. Inoue, *Phys. Rev. B* **77**, 165117 (2008).

28. M. Morota, Y. Niimi, K. Ohnishi, D. H. Wei, T. Tanaka, H. Kontani, T. Kimura, and Y.

Otani, *Phys. Rev. B* **83**, 174405 (2011).

29. J. B. S. Mendes, R. O. Cunha, O. Alves Santos, P. R. T. Ribeiro, F. L. A. Machado, R. L. Rodríguez-Suárez, A. Azevedo, and S. M. Rezende, *Phys. Rev. B* **89**, 140406(R) (2014).
30. J. Nogues and K. I. Schuller, *J. Magn. Magn. Mater*. **192**, 203 (1999).
31. H. L. Wang, C. H. Du, P. C. Hammel, and F. Y. Yang, *Phys. Rev. Lett.* **113**, 097202 (2014).
32. P. Merodio, A. Ghosh, C. Lemonias, E. Gautier, U. Ebels, M. Chshiev, H. Béa, V. Baltz, and W. E. Bailey, *Appl. Phys. Lett*. **104**, 032406 (2014).

Table I. Total number of 3*d* and 4*s* electrons (n_{3d+4s}), ISHE voltages at f = 9.65 GHz and P_{rf} = 200 mW, Gilbert damping enhancement due to spin pumping $\alpha_{sp} = \alpha_{YIG/NM} - \alpha_{YIG}$ ($\alpha_{YIG} = 8.7 \pm 0.6 \times 10^{-4}$) and the calculated interfacial spin mixing conductance, electrical resistivity, spin diffusion length, and spin Hall angle for each metal (alloy).

Bilayer/ Trilayer	n_{3d+4s}	$\lvert V_{ISHE}\rvert$	α_{sp}	$g^{\uparrow\downarrow}$ (m^{-2})	ρ (Ω m)	λ_{SD} (nm)	θ_{SH}
YIG/**Ti**	4	24.6 μV	$(1.8 \pm 0.1) \times 10^{-3}$	$(3.5 \pm 0.3) \times 10^{18}$	3.0×10^{-6}	~13.3	$-(3.6 \pm 0.4) \times 10^{-4}$
YIG/**V**	5	594 μV	$(1.6 \pm 0.1) \times 10^{-3}$	$(3.1 \pm 0.3) \times 10^{18}$	2.9×10^{-6}	14.9	$-(1.0 \pm 0.1) \times 10^{-2}$
YIG/**Cr**	6	2.55 mV	$(4.3 \pm 0.3) \times 10^{-4}$	$(8.3 \pm 0.7) \times 10^{17}$	8.3×10^{-6}	13.3	$-(5.1 \pm 0.5) \times 10^{-2}$
YIG/**Mn**	7	549 μV	$(2.3 \pm 0.2) \times 10^{-3}$	$(4.5 \pm 0.4) \times 10^{18}$	9.8×10^{-6}	10.7	$-(1.9 \pm 0.1) \times 10^{-3}$
YIG/**FeMn**	7.5	4.65 μV	$(2.5 \pm 0.2) \times 10^{-3}$	$(4.9 \pm 0.4) \times 10^{18}$	2.8×10^{-6}	3.8 [32]	$-(7.4 \pm 0.8) \times 10^{-5}$
YIG/Cu/**Py**	9.6	23.7 μV	$(3.3 \pm 0.3) \times 10^{-3}$	$(6.3 \pm 0.5) \times 10^{18}$		1.7	$(2.0 \pm 0.5) \times 10^{-2}$
YIG/Cu/**Ni**	10	39.4 μV	$(1.0 \pm 0.1) \times 10^{-3}$	$(2.0 \pm 0.2) \times 10^{18}$		3.2	$(4.9 \pm 0.5) \times 10^{-2}$
YIG/**Cu**	11	0.99 μV	$(8.1 \pm 0.6) \times 10^{-4}$	$(1.6 \pm 0.1) \times 10^{18}$	6.3×10^{-8}	500	$(3.2 \pm 0.3) \times 10^{-3}$

Figure captions:

Figure 1. (a) Semi-log 2θ-ω XRD scan of a 25-nm YIG film, which exhibits clear Laue oscillations. (b) X-ray reflectometry spectrum of a YIG(40 nm) film on GGG. Inset: AFM image of a 25-nm YIG film with a roughness of 0.106 nm. (c) A room-temperature FMR derivative spectrum of a YIG film with an in-plane field at P_{rf} = 0.2 mW, which gives ΔH = 9.5 Oe. (d) Schematic of experimental setup for ISHE measurements.

Figure 2. V_{ISHE} vs. $H - H_{res}$ spectra of (a) YIG/Ti, (b) YIG/V, (c) YIG/Cr, (d) YIG/Mn, (e) YIG/$Fe_{50}Mn_{50}$ bilayers and (f) YIG/Cu/Ni trilayer at θ_H = 90°(red) and 270° (blue) using P_{rf} = 200 mW. Cr thickness dependence of (g) ISHE voltage, (h) resistivity, and (i) ISHE-induced charge current (V_{ISHE}/R) normalized by sample width w of YIG/Cr(t_{Cr}) bilayers. A spin diffusion length of λ_{SD} = 13.3 $\pm$ 2.1 nm is obtained from (i). (j) V, (k) Mn, and (l) Ni thickness dependencies of ISHE-induced charge currents normalized by w of the YIG/V(t_V), YIG/Mn(t_{Mn}), and YIG/Ni(t_{Ni}) bilayers give λ_{SD} = 14.9 $\pm$ 2.4, 10.7 $\pm$ 1.1, and 3.2 $\pm$ 0.1 nm for V, Mn, and Ni, respectively.

Figure 3. (a) Frequency dependencies of FMR linewidth of a bare YIG film, five YIG/metal bilayers, and a YIG/Cu/Ni trilayer. (b) Z dependence of the calculated θ_{SH} of 3d transition metals shows a surprisingly large variation of θ_{SH} with n_{3d+4s}.

Figure 4. Influence of film thickness on Cr antiferromagnetism: room temperature magnetic hysteresis loops of a single YIG(20 nm) film and YIG/Cr bilayers with t_{Cr} = 10, 35, 50, and 100 nm, which give coercivities of 0.35, 0.52, 0.74, 1.26, and 1.73 Oe, respectively. The inset shows the frequency dependencies of FMR linewidth of YIG/Cr(10 nm) and YIG/Cr(100 nm).

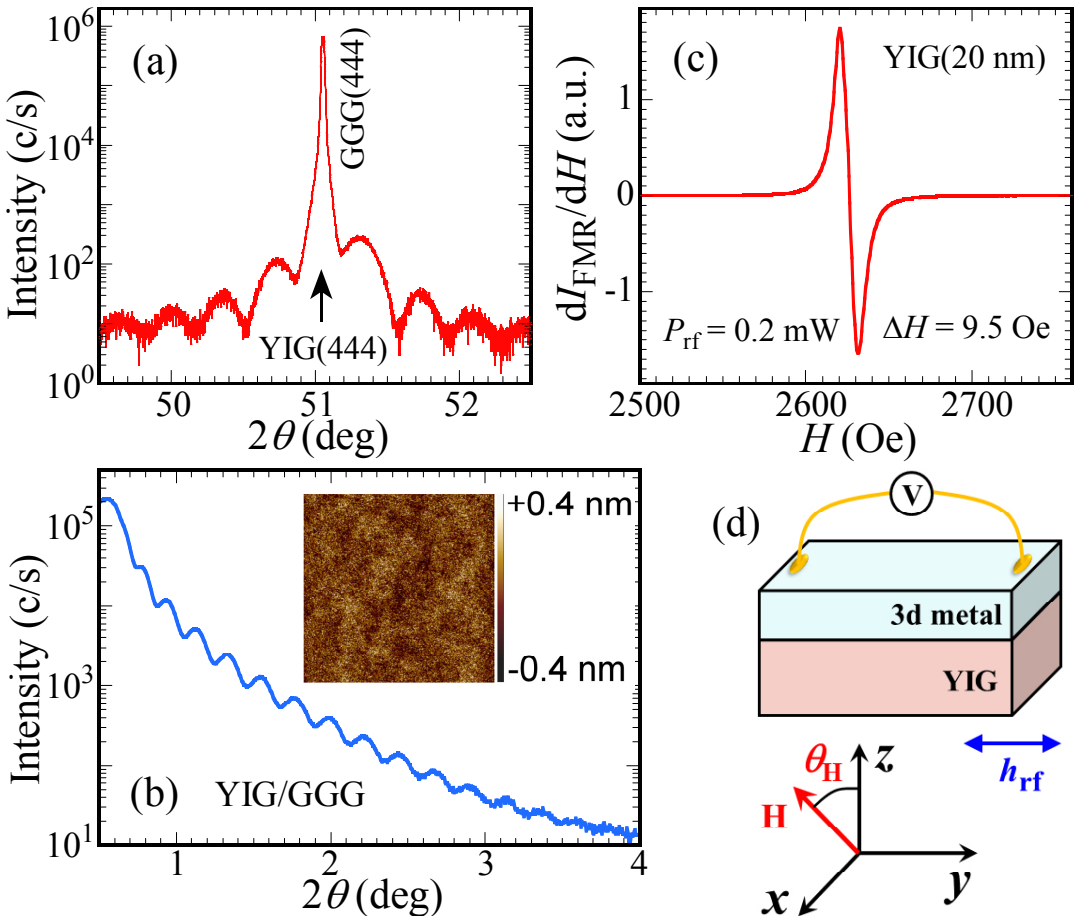
(a)
GGG(444)
YIG(444)
Intensity (c/s)
2θ (deg)
(c)
YIG(20 nm)
dI_FMR/dH (a.u.)
P_rf = 0.2 mW
ΔH = 9.5 Oe
H (Oe)
(b) YIG/GGG
+0.4 nm
-0.4 nm
Intensity (c/s)
2θ (deg)
(d)
V
3d metal
YIG
θ_H
z
H
h_rf
x
y

Figure 1

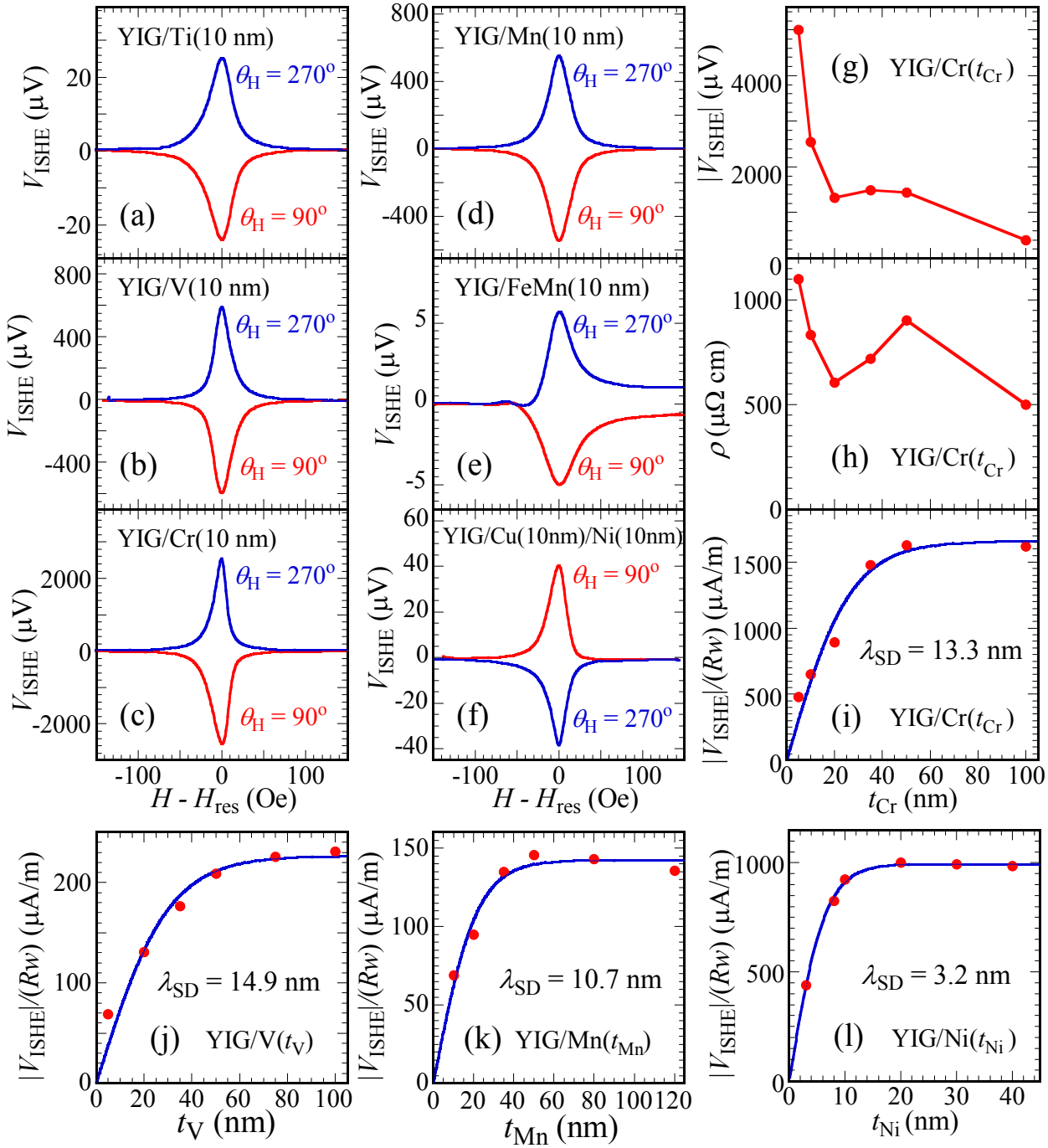
YIG/Ti(10 nm)
YIG/Mn(10 nm)
YIG/V(10 nm)
YIG/FeMn(10 nm)
YIG/Cr(10 nm)
YIG/Cu(10nm)/Ni(10nm)
θ_H = 270°
θ_H = 90°
(a)
(b)
(c)
(d)
(e)
(f)
V_{ISHE} (μV)
$H - H_{res}$ (Oe)
(g) YIG/Cr(t_{Cr})
(h) YIG/Cr(t_{Cr})
(i) YIG/Cr(t_{Cr})
$|V_{ISHE}|$ (μV)
ρ (μΩ cm)
$|V_{ISHE}|/(Rw)$ (μA/m)
λ_{SD} = 13.3 nm
t_{Cr} (nm)
(j) YIG/V(t_V)
λ_{SD} = 14.9 nm
t_V (nm)
(k) YIG/Mn(t_{Mn})
λ_{SD} = 10.7 nm
t_{Mn} (nm)
(l) YIG/Ni(t_{Ni})
λ_{SD} = 3.2 nm
t_{Ni} (nm)

Figure 2

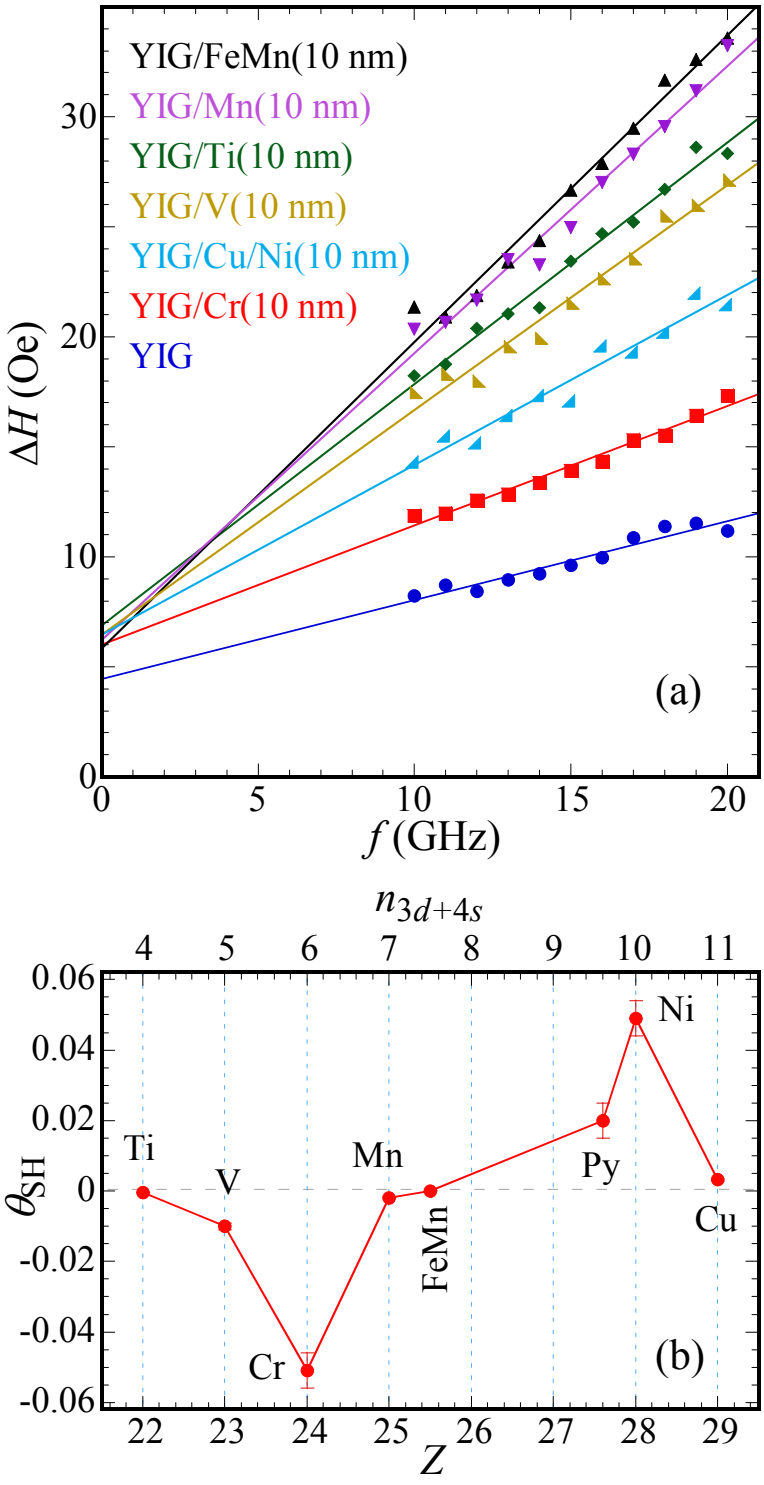
YIG/FeMn(10 nm)
YIG/Mn(10 nm)
YIG/Ti(10 nm)
YIG/V(10 nm)
YIG/Cu/Ni(10 nm)
YIG/Cr(10 nm)
YIG
ΔH (Oe)
f (GHz)
(a)
n3d+4s
θSH
Z
Ti
V
Cr
Mn
FeMn
Py
Ni
Cu
(b)

Figure 3

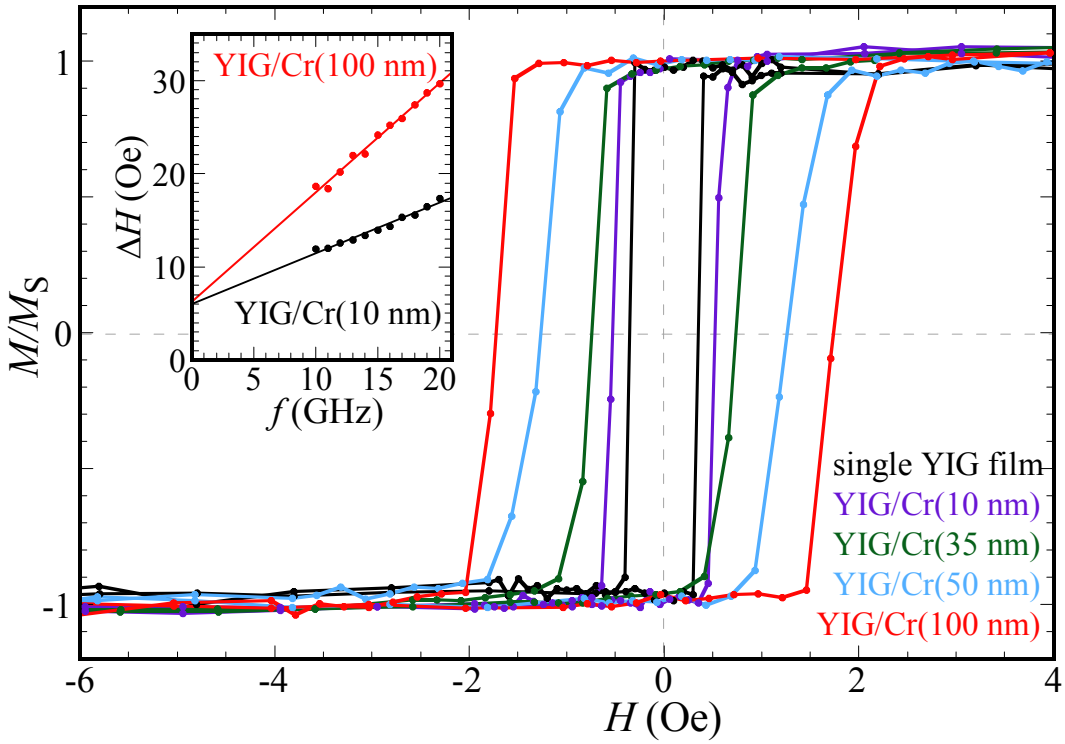
1
0
-1
M/M_S
-6
-4
-2
0
2
4
H (Oe)
single YIG film
YIG/Cr(10 nm)
YIG/Cr(35 nm)
YIG/Cr(50 nm)
YIG/Cr(100 nm)
YIG/Cr(100 nm)
YIG/Cr(10 nm)
ΔH (Oe)
0
10
20
30
0
5
10
15
20
f (GHz)

Figure 4